Strong, Lightweight and Recoverable Three-Dimensional Ceramic Nanolattices

Authors: Lucas R. Meza[1], Satyajit Das[1]†, Julia R. Greer[1, 2]*

Affiliations:

[1]Department of Engineering and Applied Science, California Institute of Technology.

[2]Kavli Nanoscience Institute, California Institute of Technology.

*Correspondence to: Julia R. Greer, email: jrgreer@caltech.edu

†Currently in the Department of Engineering, University of Cambridge

Abstract:

Ceramics have some of the highest strength- and stiffness-to-weight ratios of any material, but are sub-optimal for use as structural materials due to their brittleness and sensitivity to flaws. We demonstrate the creation of structural meta-materials comprised of nanoscale ceramics that are simultaneously ultralight, strong, energy absorbing, and can recover their original shape after compressions in excess of 50% strain. Hollow-tube alumina nanolattices were fabricated using two-photon lithography, atomic layer deposition, and oxygen plasma etching. Structures were made with wall thicknesses of 5 - 60 nm and densities of 6.3 - 258 kg/m^3. Compression experiments revealed that optimizing the wall thickness-to-radius ratio of the tubes can suppress brittle fracture in the constituent solid in favor of elastic shell buckling, resulting in ductile-like deformation and recoverability.

One Sentence Summary:

Hollow, three dimensional alumina nanolattices absorb energy and recover after substantial compression.

Main Text:

The ability to decouple properties like strength and stiffness from density requires the use of advanced processing techniques combined with materials optimized for superior mechanical performance per unit weight. Many monolithic materials with high strength-to-weight (σ_{ys}/ρ) and stiffness-to-weight (E/ρ) ratios – like technical ceramics, diamond, and metallic glasses – have excellent potential for use as strong and lightweight structural materials, but are suboptimal due to their low toughness and brittle, flaw sensitive nature. Some of these materials exhibit size effects in mechanical properties when reduced to nano-scale dimensions, like improved strength (*1*, *2*), flaw tolerance (*3*), and enhanced ductility (*4*, *5*). Architected lightweight structures made from high strength nano-ceramics (*1*, *6*, *7*) and nano-ceramic composites (*8*) have been reported to have enhanced strengths and stiffnesses, but they still suffer from brittle, catastrophic failure. Efforts to toughen fully dense brittle materials have focused primarily on using microstructural features to impede crack motion (*9–11*) and on forming composites (*12*, *13*), but these approaches have seen limited success in lightweight structures. Many natural hard materials like sea sponge skeletons (*14*) and diatom shells (*15*) are simultaneously stiff, tough, and lightweight, a combination of properties that is thought to be attained by a hierarchical design of components within their bodies (*16*).

Lightweight structures that are both strong and tough may be engineered by utilizing such hierarchical design principles. The yield strength and stiffness of cellular structures scale as $\sigma_y \propto \sigma_{ys}\bar{\rho}^n$ and $E \propto E_s\bar{\rho}^m$, where $\bar{\rho}$ is the relative density, σ_{ys} and E_s are the yield strength and stiffness of the parent solid, and exponents n and m are functions of the architecture (*17*). Cellular geometries that typically lead to highest strength are stretching-dominated, meaning they have no intrinsic mechanisms that allow for bending of the individual truss members (*18*, *19*). The yield strength and stiffness of an ideal stretching-dominated structure scale linearly with relative density as $\sigma_y \sim \bar{\rho}$ and $E \sim \bar{\rho}$ (*20*). This is in contrast to architectures that are either periodic and bending-dominated, whose modulus scales as $E \sim \bar{\rho}^2$, or stochastic, with $E \sim \bar{\rho}^3$ scaling (*21*).

We created a strong, stiff and energy absorbing hollow-tube nanolattice with an octet-truss geometry (Fig. 1) that consists solely of a brittle ceramic, aluminum oxide (alumina), and exhibits nearly full recoverability after compressions in excess of 50% strain. Nanomechanical experiments reveal that Young's modulus of our nanolattices scales with relative density as $E \sim \bar{\rho}^{1.61}$, and failure strength scales as $\sigma_f \sim \bar{\rho}^{1.76}$, which differ from the analytical scaling for both stretching- and bending-dominated structures due to the hollow tubes and nodes.

Creation of ceramic nanolattices begins with the design and writing of a 3-dimensional polymer scaffold using two-photon lithography direct laser writing. A thin alumina film is then deposited onto the polymer scaffold using atomic layer deposition (ALD) such that it coats the entire surface. The outermost walls of the coated structure are then removed using focused ion beam milling (FIB), and the internal polymer is etched away in O_2 plasma. The resulting 3-dimensional freestanding ceramic nanolattice consists of a network of hollow-tubes, as shown in Fig. 1. This fabrication method enables the creation of 3D structures with numerous geometries (*8*, *22*). Further fabrication details and a schematic of the deposition process can be found in (*23*) and are shown in Figure S1.

Nanolattices in this work were designed with relative densities spanning $\bar{\rho}$ = 0.21% to 8.6%. Using a reported value for the density of ALD alumina, ρ_s = 2900 kg/m^3 (*24*), the absolute densities of nanolattices were calculated to be ρ = 6.1 to 249 kg/m^3, which places the lightest ones into the ultralight regime, defined as materials with densities ≤ 10 kg/m^3 (*21*). This density range is comparable to that of aerogels (*25*) and other ultralight materials (*7*, *21*). In this work, nanolattices were designed to have tube wall thicknesses, t, of 5 – 60nm, tube major axis, a, of 0.45 – 1.38μm, and unit cell widths, L, of 5 – 15μm (Fig. 1, B and C), spanning length scales that can be controlled across 4 orders of magnitude. Transmission electron microscopy (TEM) analysis revealed ALD alumina to contain 2-10nm nanocrystalline precipitates intermixed in an amorphous matrix (Fig. 1F). A list of the parameters and relative densities is provided in Table S1.

Monotonic and cyclical uniaxial compression experiments were performed on nanolattices in a G200 XP Nanoindenter (Agilent Technologies). In the first set of experiments, structures were compressed uniaxially to ~50% strain at a rate of 10^{-3} s^{-1} to determine their yield stress and overall deformation characteristics (Figs. 3A-D, 4B and D, and S2A). In the second set of experiments, structures were cyclically loaded and unloaded 3 times to ~70% of their failure load, and unloading slopes from each cycle were averaged to estimate Young's modulus (Fig. 4A and C and S2B). Unloading rather than loading moduli were used to mitigate the possible effects of loading imperfections like misalignment and partial initial contact (Fig. S2B). Additional samples were compressed in an in-situ nanomechanical instrument, InSEM (Nanomechanics Inc.), to observe local and global deformation characteristics and to investigate the failure modes

that occurred during deformation (movies S1-S3). Stress-strain data and still frames of the in-situ compression experiments are shown in Figure 2.

Two distinct deformation signatures were observed during nanolattice compressions. These are best characterized using the thickness-to-radius ratio of the tubes, t/a, as a figure of merit. Structures with $t/a \geq 0.03$, referred to as thick-walled, demonstrate linear elastic loading followed by catastrophic brittle failure (Fig. 3A, B, E, and F). An example of a typical deformation and corresponding stress-strain data is shown in Figure 2F-J and movie S3. Compressive stress-strain data for thick-walled structures shows large strain bursts, with burst magnitude increasing at greater t/a; structures with $t/a = 0.032$ have bursts of ~10% strain (Fig. 3B), while structures with $t/a = 0.067$ show bursts of ~80% strain (Fig 3A). This observed increase in burst magnitude is likely driven by greater elastic strain energy stored in thicker-walled structures during deformation. Each strain burst is likely the result of a discrete brittle failure event, which leads to permanent damage of the structure (Figs. 2J, 3E and F). This type of catastrophic failure has been observed in previous experiments on hollow ceramic nanolattices (*6*), ceramic composites (*8*), and is generally typical of ceramic foams (*17*).

Thin-walled nanolattices, defined as those with $t/a \leq 0.02$, did not exhibit catastrophic failure or discrete strain bursts. Samples in this regime deformed linear elastically followed by a ductile-like, controlled deformation, with stress plateauing after yielding (Fig. 3C and D). An example of a typical deformation and corresponding stress-strain data is shown in Figure 2A-E and movie S1. As the t/a of the samples was decreased, the serrated burst behavior seen in the thick-walled structures was suppressed, and stress-strain data became smooth (Fig 3C and D). After yielding, all ensuing deformation was accommodated through wrinkling and local buckling of the tube walls (Fig 2D and E, movie S1). All thin-walled ceramic nanolattices exhibited notable recovery after deformation, with some recovering up to ~98% of their original height after compression to 50% strain (Figure 2E and 3H), and others recovering by ~80% after compression to 85% strain (Fig. S4). Structures with smaller unit cells demonstrated greater recoverability, each recovering at least 95% of its original height. Nanolattices with larger unit cells recovered less, on average to at least 75% of their original height (Figure S3). SEM images of post-deformed structures revealed localized cracking on and around the nodes (Fig. 3J), implying that the failure of ALD alumina remained brittle and that the observed deformability and recoverability likely emerged from structural effects.

Nanolattices with $0.02 \leq t/a \leq 0.03$ exhibited a combination of the two described deformation signatures. In these samples, both brittle and ductile-like deformation took place; several minor strain bursts were present, and marginal recovery occurred after compression to 50% strain (Fig 3C, G and I, movie S2). The in-situ deformation movie S2 shows that each strain burst correlates with discrete local brittle fracture events in the tubes, and post-yield ductile-like behavior corresponds to buckling and wrinkling of the tube walls. The transition between these two deformation modes is likely driven by an energetic competition between elastic and brittle failure.

Three competing failure mechanisms exist for hollow tube lattice structures: fracture of the tube wall, Euler(beam) buckling of a truss member, and local (shell) buckling of the tube wall (*26*). We define a failure mechanism (or failure mode) here to be any event that causes a loss of structural integrity of the nanolattice. Different combinations of these mechanisms can occur during deformation depending on the stress state that arises in the beams during loading. Elastic deformation and potentially recoverability will occur in a structure when the stress

necessary to initiate these processes is below the critical stress required for fracture. The condition for elastic deformation can be determined by calculating the transition point between two pairs of failure modes: shell buckling vs fracture, and Euler buckling vs fracture. Equating the stresses necessary to initiate each individual failure mechanism, we obtain an expression for the critical transition point between fracture and elastic failure (see (*23*) for full derivation):

$$\left(\frac{t}{a}\right)_{crit} = \frac{\sigma_{fs}}{E}\sqrt{3(1-\nu^2)} \quad (1)$$

$$\left(\frac{a}{L}\right)_{crit} = \frac{3}{\pi}\sqrt{\frac{2}{5}\frac{\sigma_{fs}}{E}} \quad (2)$$

Both of these functions depend on the constituent material properties: Young's modulus (E), fracture strength (σ_{fs}) and Poisson's ratio (ν). Eq. 1 represents the critical ratio between the wall thickness (t) and the major radius (a) that is necessary to induce a transition between local buckling and fracture in the tubes. Eq. 2 represents the critical ratio between the major radius (a) and length (L) of the tubes that describes a similar transition from Euler buckling to fracture.

Using mechanical property data reported for 75nm thick ALD alumina, E = 164 GPa, σ_{fs} = 1.57-2.56 GPa and ν = 0.24 (*27*), and Eqs. 1 and 2, the critical thickness-to-radius ratio that induces a transition from yielding to shell buckling in the nanolattices was calculated to be $(t/a)_{crit} \approx 0.0161 - 0.0262$, and the critical radius-to-length ratio that denotes transition from yielding to Euler buckling was $(a/L)_{crit} \approx 0.0591 - 0.0755$. The property space of all nanolattices studied here, along with their t/a, a/L, and predicted failure modes, are shown in Table S1. The experimentally observed deformation behavior of each sample is also noted in the table.

The radius-to-length ratios, a/L, for nanolattices studied here ranged from 0.0750 to 0.180. All of these values are greater than or equal to $(a/L)_{crit}$ predicted by Eq. 2, which means that in an ideal structure, the beams will fracture before the Euler buckling condition is met. This prediction is consistent with our experimental results; no Euler buckling was observed in our in-situ compression experiments (Fig 2, movies S1 – S3). This model is not capable of capturing local-scale stress concentrations, nor does it account for structures with a high degree of misalignment or pre-bending of the beams, which have been reported to reduce the critical load required to initiate buckling (*6*). The a/L values of the nanolattices are close to $(a/L)_{crit}$, suggesting that Euler buckling may occur in the samples with a large degree of misaligned or pre-bent beams, but it is not observed experimentally to be a dominant deformation mechanism.

The thickness-to-diameter ratios, t/a, of the nanolattices ranged from 0.0059 to 0.0862, which overlaps the range of $(t/a)_{crit}$ predicted by Eq. 1. For thick-walled structures, whose $t/a \geq 0.030 > (t/a)_{crit}$, the model predicts that failure of the beams is dominated by brittle fracture within the alumina tubes. Fractured segments of tubes are unable to carry any load, so every failure event will cause a strain burst whose magnitude depends on the amount of strain energy stored in the system prior to failure. These predictions are corroborated by experimental stress-strain data for the thick walled structures (Figs. 2I and J, 3E and F, and Movie S3).

Failure in the thin-walled structures, whose $t/a \leq (t/a)_{crit} \leq 0.020$, is predicted to occur primarily via shell buckling, which is an elastic failure mode. This type of failure corresponds to a plateau in the stress-strain data caused by a gradual drop in load carrying capacity of the beams (*28*), in contrast to the immediate drop in load carrying capacity associated with fracture.

Bending of an isolated thin-walled hollow beam often leads to shell buckling bifurcation, which can cause a jump in displacement (*29*). In a truss structure, the interactions and nodal support among all the beams delays the onset of bifurcation and allows the beams to gradually settle into a new mode. Shell buckling in thin-walled nanolattices is manifested as wrinkling and warping of the tubes near the nodes (Figs. 2D and E, 3H and J and movie S1). The ductile-like deformation and recoverability observed in our experiments on the thin-walled nanolattices likely arise as a result of such shell buckling.

The proposed shell buckling model does not take into account the microstructural or material details, nor is it capable of predicting the deformation of structures in the transition regime of $0.020 \leq t/a \leq 0.030$. It is helpful in qualitatively explaining deformation in this regime, where nanolattices experience a complex stress state with compressive, tensile, and shear components. Fracture occurs primarily under tension and shear and buckling occurs only in compression, which means that the stress state within the beams can simultaneously satisfy fracture and buckling conditions. This is observed experimentally as a mixing of fracture and buckling failure modes, along with suppressed strain burst behavior and some recoverability (Fig. 3G and I and Movie S2).

Elastic recovery has been studied previously in metallic and polymer lattices, and models have been proposed for their recoverability (*21*, *30–32*). None of these works account for the observed ductile-like behavior of the ceramic nanolattices, and elastically deformable structures comprised of intrinsically brittle materials like ceramics are virtually unexplored. We postulate that reducing the t/a ratio to below $(t/a)_{crit}$ derived in Eq. 1 enables failure via shell buckling, an elastic failure mode that causes minimal damage to the beams and nodes and allows the structure to recover. The transition to elastic failure is a necessary condition to prevent initial yielding or fracture of the constituent material but not a sufficient condition to ensure recovery of the structure. Figure 2D shows that during shell buckling, the global deformation is accompanied by localized wrinkling and warping of the tube walls. This results in confined regions of high stress that can subsequently lead to localized fracture (Fig. 2E and 3J). The propagation of these localized micro-cracks depends on the overall stress landscape and flaw distribution. If a crack extends into a region of high tensile stresses, or if numerous flaws reside near a crack tip, it will likely propagate through the node and can potentially result in fracture of the tube. If an existing crack extends into a region of compressive stress, or if the stress field is insufficient to continue the crack extension, its propagation will be suppressed such that the tubes may never fully fracture. In this mechanism, a sufficient number of nodal connections remain intact to enable the structure to recover nearly fully to its original shape. The applied compressive load reduces the local tensile stresses within the tube walls that are generated by bending of the beams, which generates a compressive stress state at the nodes that can impede the propagation of a crack. As the t/a is reduced, shell buckling will commence at a lower applied load (Eq. 1), which lowers the probability of initiating and/or propagating an existing crack. The wall thicknesses of alumina are on the order of tens of nanometers, a length scale that has been shown to exhibit enhanced strengths and damage tolerance caused by a statistically lower probability of finding a weak defect (*1*). These are some of the phenomena that collectively give rise to recoverability of the alumina nanolattices (Figs. 2E, 3H, S3 and S4).

We discovered that the strength and Young's modulus of all our octet-truss nanolattices follow a power law scaling with relative density as $\sigma_y \sim \bar{\rho}^{1.76}$ and $E \sim \bar{\rho}^{1.61}$ (Figure 4A and B). This scaling outperforms traditional lightweight and ultralight bending-dominated structural

materials, whose properties that scale as $E \sim \bar{\rho}^{2}$ or $E \sim \bar{\rho}^{3}$ (*21*), but does not follow the analytic prediction for an ideal stretching-dominated structure, $\sigma_{ys} \sim \bar{\rho}$ and $E \sim \bar{\rho}$ (*20*). Such a deviation from the analytic prediction can be explained, in part, by factors like the ellipticity of the tubes, structural imperfections, and non-idealities of the experimental setup. We attribute this deviation primarily to the hollowness of the tubes, which affects the structural integrity of the nodes, where the highest stress concentrations will occur (*30*, *31*).

The strength and deformation of an ideal, monolithic stretching-dominated cellular solid is governed by stretching of the beams, with the nodes acting as rigid, pin-jointed elements that perfectly transfer load between truss members (*20*). In a hollow lattice, the nodes are constrained only by the shell walls, which has a detrimental effect on strength and stiffness because load transfer at the nodes occurs via shell wall bending. This, together with the sharp angles between the tubes, leads to an uneven distribution of stress and induces large stress concentrations in the vicinity of the nodes (Fig 1B and E). Bending of the tubes also causes large deflections and additional ovalisation at the nodes, which further increases the compliance and stress concentrations. In-situ experiments and post-compression analysis revealed that most of the deformation is localized to the nodes (Fig. 2D, E, and 3J), which implies that improving nodal strength is a critical factor in enhancing the scaling of strength and stiffness with density.

We demonstrate the creation of ultralight, hollow ceramic nanolattices that absorb energy, recover after significant compression, and reach an untapped strength and stiffness material property space. This is achieved using high-strength ALD alumina engineered into a thin-walled nanolattice that is capable of deforming elastically via shell buckling. The ultralight ceramic nanolattices represent the concept of "materials by design", where it is possible to transform a strong and dense brittle ceramic into a strong, ultralight, energy absorbing and recoverable meta-material. These results serve to emphasize the critical connection between material microstructure, hierarchical architecture, and mechanical properties at relevant length scales.

References:

1. D. Jang, L. R. Meza, F. Greer, J. R. Greer, Fabrication and deformation of three-dimensional hollow ceramic nanostructures, *Nat. Mater.* **12**, 893–898 (2013).

2. J. R. Greer, J. T. M. De Hosson, Plasticity in small-sized metallic systems: Intrinsic versus extrinsic size effect, *Prog. Mater. Sci.* **56**, 654–724 (2011).

3. X. W. Gu, Z. Wu, Y.-W. Zhang, D. J. Srolovitz, J. R. Greer, Microstructure versus flaw: mechanisms of failure and strength in nanostructures, *Nano Lett.* **13**, 5703–5709 (2013).

4. D. Z. Chen *et al.*, Nanometallic glasses: size reduction brings ductility, surface state drives its extent, *Nano Lett.* **13**, 4462–4468 (2013).

5. J. Rys *et al.*, Fabrication and Deformation of Metallic Glass Micro-Lattices, *Adv. Eng. Mater.* (2014), doi:10.1002/adem.201300454.

6. L. R. Meza, J. R. Greer, Mechanical characterization of hollow ceramic nanolattices, *J. Mater. Sci.* **49**, 2496–2508 (2013).

7. X. Zheng *et al.*, Ultralight, ultrastiff mechanical metamaterials, *Science (80-.).* **344**, 1373–1377 (2014).

8. J. Bauer, S. Hengsbach, I. Tesari, R. Schwaiger, O. Kraft, High-strength cellular ceramic composites with 3D microarchitecture, *Proc. Natl. Acad. Sci.* **111**, 2453–2458 (2014).

9. A. G. Evans, Perspective on the Development of High-Toughness Ceramics, *J. Am. Ceram. Soc.* **73**, 187–206 (1990).

10. I.-W. Chen, L. A. Xue, Development of Superplastic Structural Ceramics, *J. Am. Ceram. Soc.* **73**, 2585–2609 (1990).

11. P. F. Becher, Microstructural Design of Toughened Ceramics, *J. Am. Ceram. Soc.* **74**, 255–269 (1991).

12. D. C. Hofmann *et al.*, Designing metallic glass matrix composites with high toughness and tensile ductility, *Nature* **451**, 1085–1090 (2008).

13. E. Munch *et al.*, Tough, bio-inspired hybrid materials, *Science* **322**, 1516–1520 (2008).

14. J. C. Weaver *et al.*, Hierarchical assembly of the siliceous skeletal lattice of the hexactinellid sponge Euplectella aspergillum, *J. Struct. Biol.* **158**, 93–106 (2007).

15. C. E. Hamm *et al.*, Architecture and material properties of diatom shells provide effective mechanical protection, *Nature* **421**, 841–843 (2003).

16. M. A. Meyers, J. McKittrick, P.-Y. Chen, Structural biological materials: critical mechanics-materials connections, *Science* **339**, 773–779 (2013).

17. L. J. Gibson, M. F. Ashby, *Cellular Solids: Structure and Properties* (Cambridge University Press, Cambridge, ed. 2, 1999).

18. V. S. Deshpande, M. F. Ashby, N. A. Fleck, Foam topology: bending versus stretching dominated architectures, *Acta Mater.* **49**, 1035–1040 (2001).

19. S. Pellegrino, C. R. Calladine, Matrix Analysis of Statically and Kinematically Indeternimate Frameworks, *Int. J. Solids Struct.* **22**, 409–428 (1986).

20. V. S. Deshpande, N. A. Fleck, M. F. Ashby, Effective properties of the octet-truss lattice material, *J. Mech. Phys. Solids* **49**, 1747–1769 (2001).

21. T. A. Schaedler *et al.*, Ultralight metallic microlattices, *Science* **334**, 962–965 (2011).

22. L. C. Montemayor, L. R. Meza, J. R. Greer, Design and Fabrication of Hollow Rigid Nanolattices via Two-Photon Lithography, *Adv. Eng. Mater.* **16**, 184–189 (2014).

23. Supplementary Materials.

24. M. D. Groner, F. H. Fabreguette, J. W. Elam, S. M. George, Low-temperature Al2O3 Atomic Layer Deposition, *Chem. Mater.* **16**, 639–645 (2004).

25. Y. K. Akimov, Field of Application of Aerogels (Review), *Instruments Exp. Tech.* **46**, 287–299 (2003).

26. L. Valdevit, A. J. Jacobsen, J. R. Greer, W. B. Carter, T. M. Pollock, Ed. Protocols for the Optimal Design of Multi-Functional Cellular Structures: From Hypersonics to Micro-Architected Materials, *J. Am. Ceram. Soc.* **94**, s15–s34 (2011).

27. M. Berdova *et al.*, Mechanical assessment of suspended ALD thin films by bulge and shaft-loading techniques, *Acta Mater.* **66**, 370–377 (2014).

28. H. G. Allen, P. S. Bulson, *Background to buckling* (McGraw-Hill Book Company, Berkshire, England, 1980).

29. G. Ju, S. Kyriakides, Bifurcation and localization instabilities in cylindrical shells under bending—II. Predictions, *Int. J. Solids Struct.* **29**, 1143–1171 (1992).

30. A. Torrents, T. A. Schaedler, A. J. Jacobsen, W. B. Carter, L. Valdevit, Characterization of nickel-based microlattice materials with structural hierarchy from the nanometer to the millimeter scale, *Acta Mater.* **60**, 3511–3523 (2012).

31. L. Valdevit, S. W. Godfrey, T. a. Schaedler, A. J. Jacobsen, W. B. Carter, Compressive strength of hollow microlattices: Experimental characterization, modeling, and optimal design, *J. Mater. Res.* **28**, 2461–2473 (2013).

32. K. J. Maloney *et al.*, Microlattices as architected thin films: Analysis of mechanical properties and high strain elastic recovery, *APL Mater.* **1**, 022106 (2013).

33. M. Ritala *et al.*, Perfectly conformal TiN and Al2O3 films deposited by atomic layer deposition, *Chem. Vap. Depos.* **5**, 7–9 (1999).

Acknowledgments:

The authors gratefully acknowledge the financial support from the Defense Advanced Research Projects Agency under the MCMA program managed by J. Goldwasser (contract no. W91CRB-10-0305) and to the Institute for Collaborative Biotechnologies through grant W911NF-09-0001 from the U.S. Army Research Office. The content of the information does not necessarily reflect the position or the policy of the Government, and no official endorsement should be inferred. The authors are grateful to the Kavli Nanoscience Institute at Caltech for the availability of critical cleanroom facilities, and to Rachel Liontas and Carol Garland for TEM assistance. Part of this work was carried out in the Lewis Group facilities at Caltech.

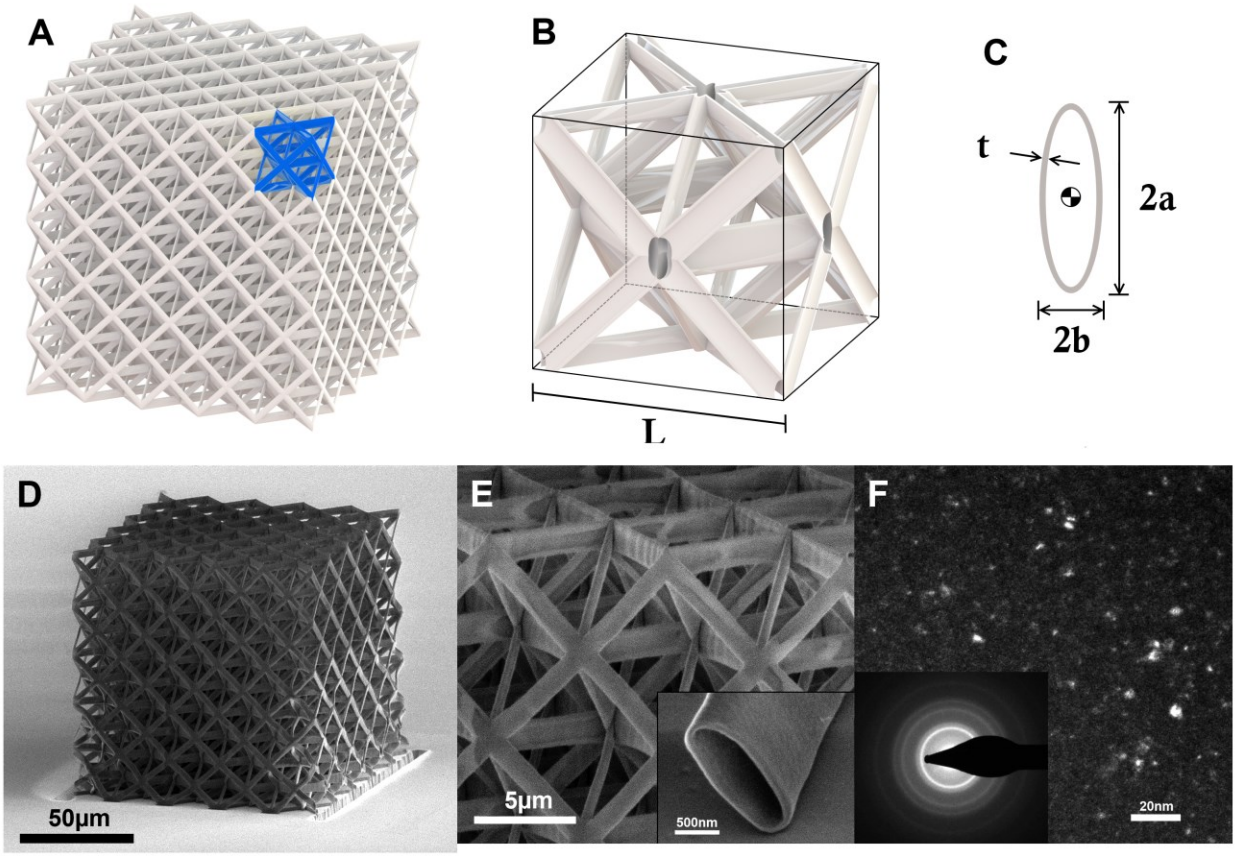

Fig. 1: Architecture, design, and microstructure of alumina nanolattices. *(**A**) CAD image of the octet-truss design used in the study. The blue section represents a single unit cell. (**B**) Cut-away of hollow octet-truss unit cell. (**C**) Hollow elliptical cross-section of a nanolattice tube. (**D**) SEM image of alumina octet-truss nanolattice. (**E**) Zoomed in section of the alumina octet-truss nanolattice. The inset shows an isolated hollow tube. (**F**) TEM dark field with diffraction grating of the alumina nanolattice tube wall.*

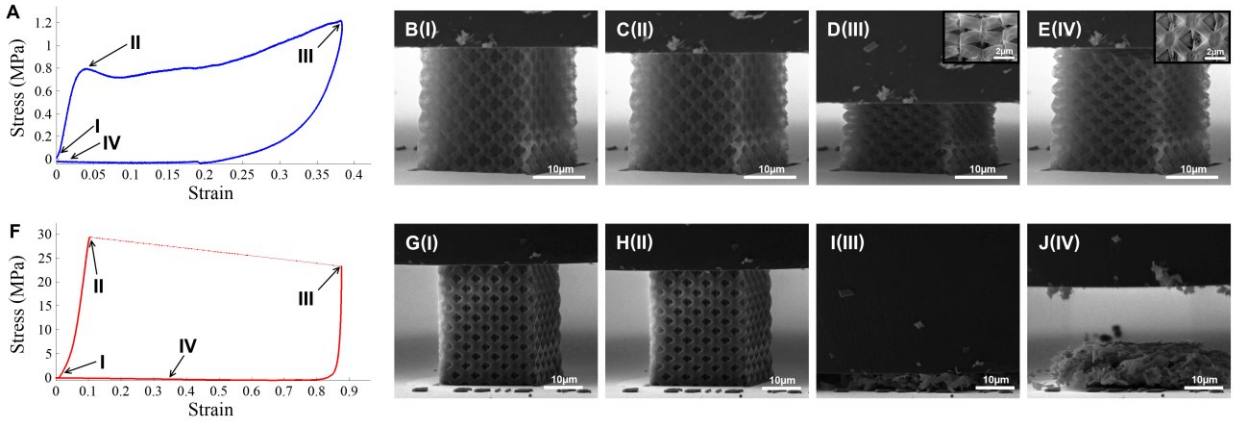

Fig. 2: Compression experiments on thick- and thin-walled nanolattices. *(**A-E**) Mechanical data and still frames from the compression test on a thin-walled (L=5μm, a=650nm, t=10nm) nanolattice demonstrating the slow, ductile-like deformation, local shell buckling, and recovery of the structure post-compression. (**F-J**) Mechanical data and still frames from the compression test on a thick-walled (L=5μm, a=790nm, t=50nm) nanolattice showing catastrophic brittle failure and no post-compression recovery.*

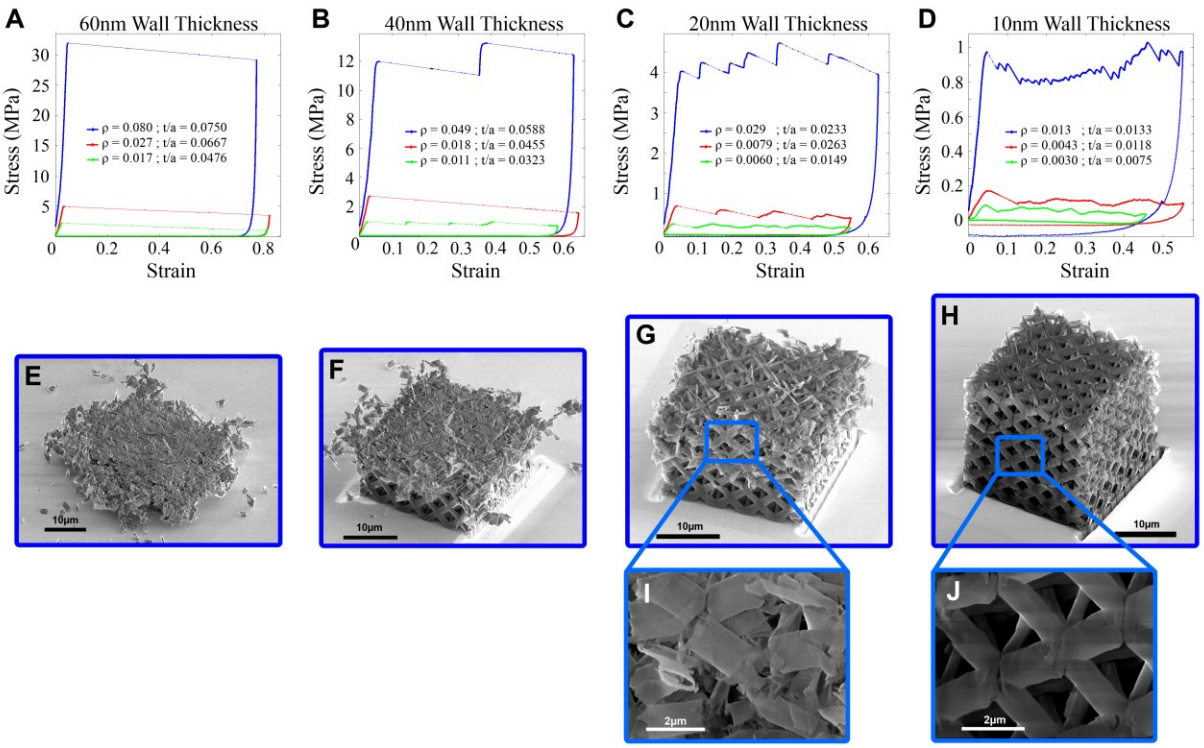

Fig. 3: Mechanical tests on varying wall thickness and relative density samples. *(**A-D**) Stress-strain plots of varying wall thickness structures showing the transition from brittle to ductile-like deformation with thinner walled structures. (**E-J**) Post-compression images of the nanolattices showing the recoverability as wall thickness is reduced.*

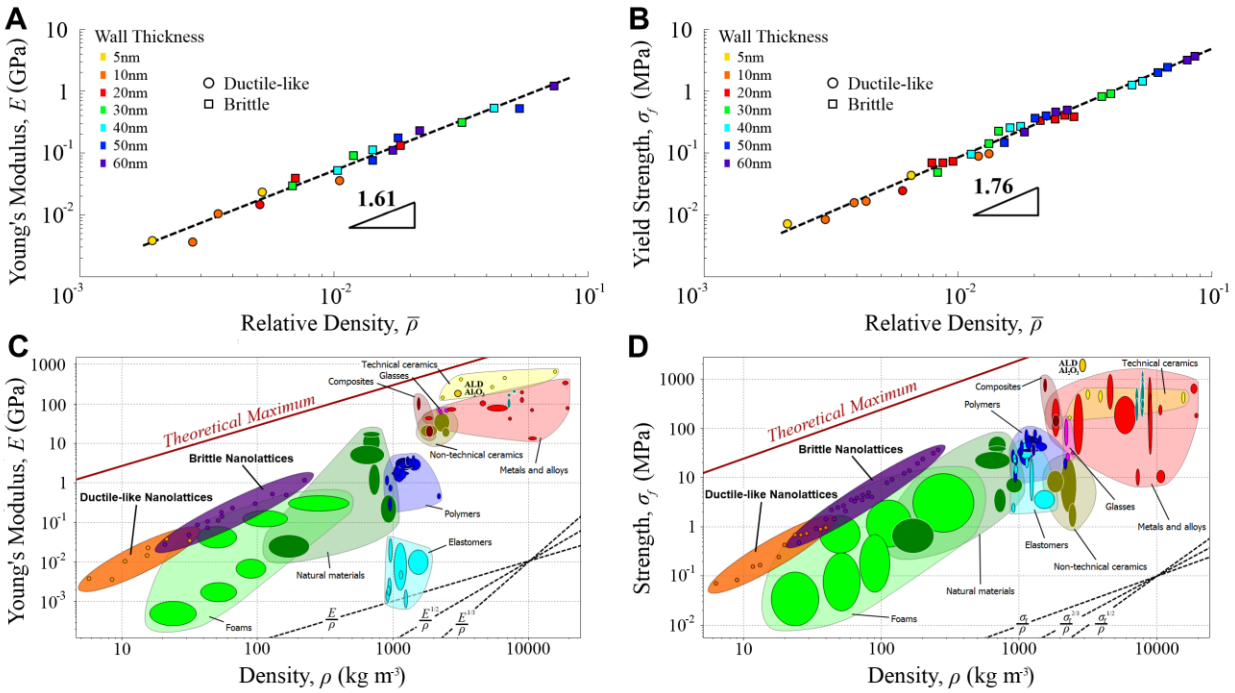

Fig. 4: Strength and stiffness vs. density of alumina nanolattices. *(**A-B**) Stiffness and strength plotted against relative density for all the samples tested. There is a clear power law fit for the data, with no deviation across wall thicknesses or failure modes. (**C-D**) Material property plots (CES Selector) of the experimental stiffness and strength data against existing materials, showing that the materials in these experiments are able to reach a new parameter space of high strength and stiffness lightweight materials.*

Supplementary Materials:

Materials and Methods

Figures S1-S6

Table S1

Movies S1-S3

References (*1-33*)